

Magnetic field induced quantum spin liquid in $\text{K}_2\text{Ni}_2(\text{SO}_4)_3$ comprising two interpenetrated trillium lattices

Ivica Živković,^{1,*} Virgile Favre,¹ Catalina Salazar Mejia,² Harald O. Jeschke,³ Arnaud Magrez,⁴ Bhupen Dabholkar,⁵ Vincent Noculak,^{6,7} Rafael S. Freitas,⁸ Minki Jeong,⁹ Nagabhushan G. Hegde,¹ Luc Testa,¹ Peter Babkevich,¹ Yixi Su,¹⁰ Pascal Manuel,¹¹ Hubertus Luetkens,¹² Christopher Baines,¹² Peter J. Baker,¹¹ Jochen Wosnitza,^{2,13} Oksana Zaharko,¹⁴ Yasir Iqbal,¹⁵ Johannes Reuther,^{6,7} and Henrik M. Rønnow¹

¹Laboratory for Quantum Magnetism, Institute of Physics,
École Polytechnique Fédérale de Lausanne, CH-1015 Lausanne, Switzerland

²Hochfeld-Magnetlabor Dresden (HLD-EMFL) and Würzburg-Dresden Cluster of Excellence ct.qmat,
Helmholtz-Zentrum Dresden-Rossendorf, 01328 Dresden, Germany

³Research Institute for Interdisciplinary Science, Okayama University, Okayama 700-8530, Japan

⁴Crystal Growth Facility, Ecole Polytechnique Fédérale de Lausanne, Lausanne, Switzerland.

⁵Department of Physics, Indian Institute of Technology Madras, Chennai 600036, India

⁶Dahlem Center for Complex Quantum Systems and Fachbereich Physik,
Freie Universität Berlin, 14195 Berlin, Germany

⁷Helmholtz-Zentrum für Materialien und Energie, Hahn-Meitner-Platz 1, 14109 Berlin, Germany

⁸Instituto de Física, Universidade de São Paulo, 05508-090, São Paulo, Brazil

⁹School of Physics and Astronomy, University of Birmingham, Edgbaston, Birmingham, B15 2TT UK

¹⁰Jülich Centre for Neutron Science (JCNS) at Heinz Maier-Leibnitz Zentrum (MLZ),

Forschungszentrum Jülich, Lichtenbergstrasse 1, D-85747 Garching, Germany

¹¹ISIS Pulsed Neutron and Muon Source, STFC Rutherford Appleton Laboratory,
Harwell Science and Innovation Campus, Didcot, Oxfordshire, OX11 0QX UK

¹²Laboratory for Muon Spin Spectroscopy, Paul Scherrer Institute, CH-5232 Villigen, Switzerland

¹³Institut für Festkörper- und Materialphysik, TU Dresden, 01062 Dresden Germany

¹⁴Laboratory for Neutron Scattering and Imaging,
Paul Scherrer Institut, CH-5253 Villigen, Switzerland

¹⁵Department of Physics and Quantum Centers in Diamond and Emerging Materials (QuCenDiEM) group,
Indian Institute of Technology Madras, Chennai 600036, India

(Dated: August 6, 2021)

METHODS

Sample preparation

The powder of $\text{K}_2\text{Ni}_2(\text{SO}_4)_3$ was prepared by solid state reaction from a stoichiometric mixture of K_2SO_4 and $\text{NiSO}_4 \cdot 6\text{H}_2\text{O}$ annealed at 450°C for five days. The powder is quenched to room temperature and stored in a desiccator as $\text{K}_2\text{Ni}_2(\text{SO}_4)_3$ is mildly sensitive to moisture. High quality single crystals were obtained by sealing the powder in an evacuated quartz ampoule. Millimeter sized crystals are obtained by cooling the melt from 850°C to 750°C at a 1 K/h rate.

Single-crystal x-ray diffraction

A small single crystal of $\text{K}_2\text{Ni}_2(\text{SO}_4)_3$ has been glued onto the tip of a glass needle and cooled down to 100 K with a flow of cold nitrogen gas. Data has been collected on a Rigaku SuperNOVA diffractometer using Mo/Cu Duo source with Atlas CCD.

Magnetization and magnetic susceptibility

Magnetization M and magnetic susceptibility $\chi_{\text{DC}} = M/B$ of powder and single crystal samples were measured using a commercial superconducting quantum interference device magnetometer MPMS-5T (Quantum Design).

Heat capacity

Heat capacity measurements above 2 K were performed on powder and single crystal samples using a commercial PPMS (Quantum Design). Below 2 K, a home-made setup using a dilution refrigerator has been used to measure single crystal sample. In both cases a short (1-3 %) heat pulse method has been utilized.

Muon spin relaxation (μSR)

μSR experiments were performed on powder samples at MUSR, ISIS (UK) and LTF/GPS, PSI (Switzerland) beamlines using the spin-polarized positive muons (μ^+).

Neutron diffraction

Neutron diffraction on powder was performed on the time-of-flight diffractometer WISH, ISIS (UK). For temperatures below 1 K, a copper can was attached to a dilution refrigerator and filled with 15 g of powder. Above 1 K, a vanadium can was used with 15 g of powder in a helium-flow environment.

Spin-polarized neutron diffraction and inelastic neutron scattering

Both spin-polarized neutron diffraction and non-polarized time-of-flight (TOF) inelastic neutron scattering measurements were carried out at the polarized spectrometer DNS at the Heinz Maier-Leibnitz Zentrum (MLZ), Garching, Germany. Approximately 2 g of powder were enclosed in an annular cylinder sample holder made with oxygen-free copper and sealed in a He atmosphere. Measurements were taken in a ^3He insert installed in a top-loading CCR cryostat. A neutron wavelength at $\lambda = 4.2 \text{ \AA}$ was chosen for both measurements. The magnetic scattering cross-section was obtained via the XYZ polarization analysis method, for which the standard procedures such as flipping-ratio correction and normalisation of detector efficiency have been applied. The TOF inelastic neutron scattering data were taken with a disc chopper running at 250 Hz, which yields an energy resolution at $\sim 0.25 \text{ meV}$ at 4.2 \AA . The runs for both vanadium and empty copper sample can were undertaken under the same TOF condition. The powder-average inelastic scattering profiles were obtained via Mantid-based data reduction routines.

Density functional theory

We study $\text{K}_2\text{Ni}_2(\text{SO}_4)_3$ using density functional theory (DFT) calculations based on the full potential local orbital (FPLO) basis set [1] combined with the generalized gradient approximation (GGA) to the exchange correlation functional [2] and with a GGA+ U correction for the strongly correlated Ni^{2+} $3d$ orbitals [3]. We employ the energy mapping technique [4, 5] to extract the Heisenberg exchange interactions up to a Ni-Ni distance of 8.6 Å from 20 GGA+ U total energies of selected spin configurations in a $\sqrt{2} \times \sqrt{2} \times 1$ supercell. We fix the Hund's rule coupling at $J_{\text{H}} = 0.88$ eV following Ref. [6].

PFFRG

The model Hamiltonian for $\text{K}_2\text{Ni}_2(\text{SO}_4)_3$ with the Heisenberg exchange interactions obtained from DFT is further studied within the pseudofermion functional renormalization group (PFFRG) method. [7] This approach is based on a fermionic rewriting of the spin operators, where a spin-1 is represented by two coupled spin-1/2 degrees of freedom. [8] The resulting fermionic theory is then treated with many-body Feynman diagram approaches. Particularly, via the introduction of an infrared frequency cutoff, the fermionic vertex functions are subject to a renormalization group flow as described within the standard functional renormalization group (FRG) scheme. [9, 10] We solve the corresponding differential equations in real space on a one-loop level, by taking into account spin-spin correlations up to a distance of twice a lattice vector of the underlying cubic lattice and approximate the frequency dependence of the vertex functions by 64 discrete mesh points. The central outcome is the zero-frequency, momentum-resolved real part of the magnetic susceptibility $\chi'(Q)$ which is obtained from the fermionic two-particle vertex. Using Kramers-Kronig relations, $\chi'(Q)$ is related to the dynamical spin structure factor $S(Q, \omega)$ via

$$\chi'(Q) \propto \int d\omega S(Q, \omega)/\omega, \quad (\text{S1})$$

indicating that $\chi'(Q)$ primarily represents the low-energy contribution of $S(Q, \omega)$. Most importantly, $\chi'(Q)$ takes into account quantum fluctuations well beyond mean field and is, hence, well suited to simulate the fluctuating moments of $\text{K}_2\text{Ni}_2(\text{SO}_4)_3$. Furthermore, possible instability signatures during the renormalization group flow allow one to detect static magnetic long-range order.

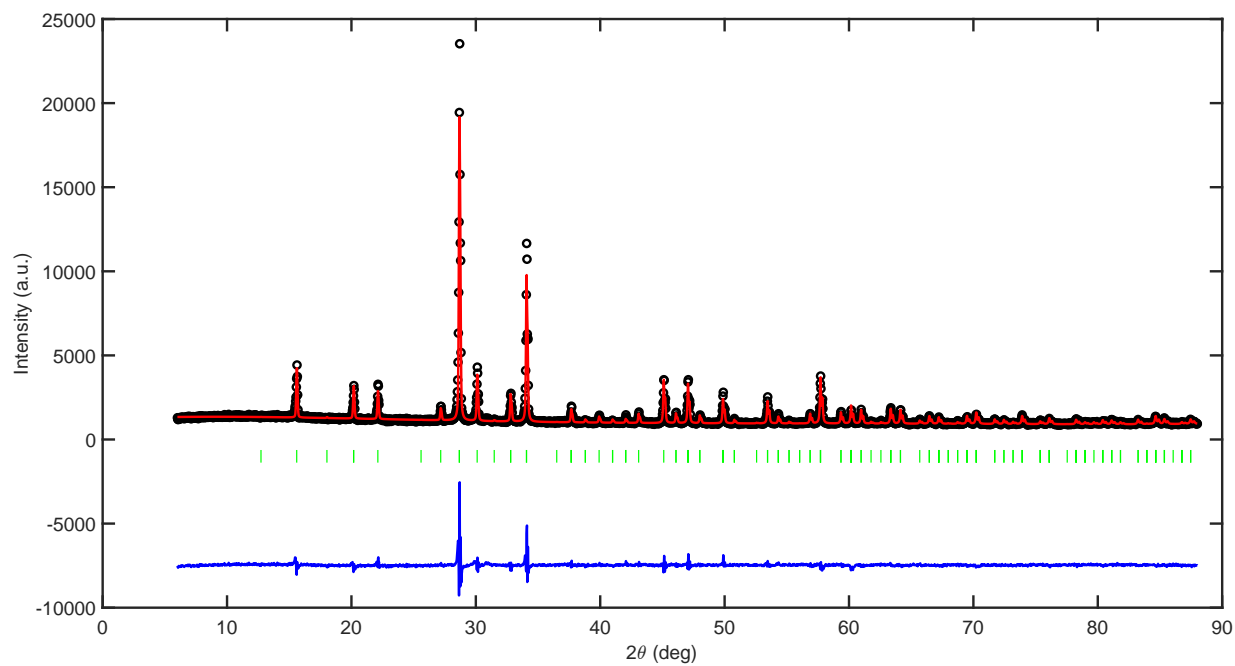
Classical Monte Carlo

Monte Carlo simulations are performed for classical Heisenberg spins on the bi-trillium lattice with periodic boundary conditions for a system of $8L^3$ spins. We employ the single-flip metropolis update with 5 over-relaxation steps added after every sweep of the lattice, and 10^4 Monte Carlo sweeps are used for thermalization. This is followed by 10^5 Monte Carlo sweeps during which measurements are performed every 10 Monte Carlo sweeps. The calculations for magnetization as a function of applied field shown in Fig. 2(b) of the main text are performed for a lattice size of $L = 8$ (4096 spins).

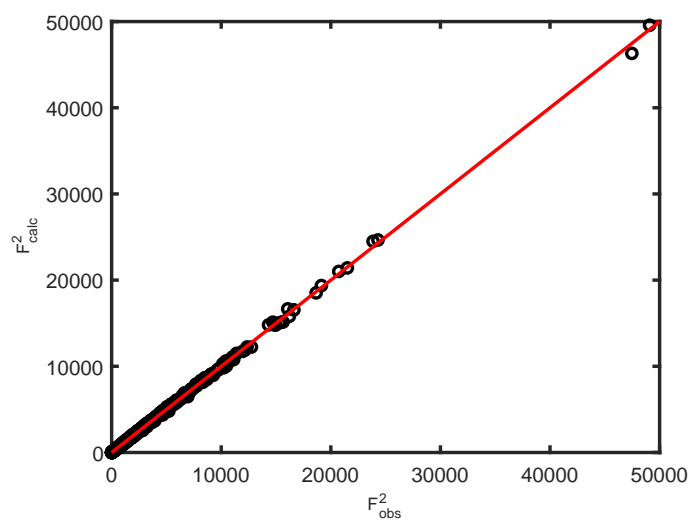
X-RAY DIFFRACTION

Powder x-ray diffraction of $\text{K}_2\text{Ni}_2(\text{SO}_4)_3$ at room temperature is presented in Fig. S1. The agreement is very good ($R_{wp} = 6.2$ %), with no visible traces of impurities.

The experimental versus calculated structure factors for a single crystal of $\text{K}_2\text{Ni}_2(\text{SO}_4)_3$ is shown in Fig. S2. The tight distribution of the data around the red line $F_{obs}^2 = F_{calc}^2$ indicates the high quality of the refinement. Additional refinement parameters are given in the supplementary Table 1. The agreement factors and the goodness-of-fit value confirm the high accuracy of the $\text{K}_2\text{Ni}_2(\text{SO}_4)_3$ structure description. Atomic positions as well as distances and angles are listed in supplementary Table 2 and 3, respectively.



Supplementary Figure S1. Powder diffraction of $K_2Ni_2(SO_4)_3$ (black circles) with the result of a Rietveld refinement (red line). The difference between the measured intensities and the fit is given with the blue line. Peak positions are marked with green vertical lines.



Supplementary Figure S2. Experimental structure factors are plotted against the calculated structure factors obtained by single crystal structure refinement of $K_2Ni_2(SO_4)_3$.

Temperature	100.01(10) K
Crystal system, space group	Cubic, P2(1)3
a = b = c	9.81866(12) Å
Volume	946.58(4) Å ³
Z, Calculated density	3, 3.395 g/cm ³
Absorption coefficient	5.589 mm ⁻¹
F(000)	952
Theta range for data collection	3.594 to 30.444 deg
Limiting indices	-5 ≤ h ≤ 14, -9 ≤ k ≤ 14, -14 ≤ l ≤ 13
Reflections collected / unique	4119 / 965 R(int) = 0.0274
Completeness to $\theta = 25.242$	98.8 %
Data / restraints / parameters	965 / 0 / 59
Goodness-of-fit on F ²	1.046
Final R indices I > 2σ(I)	R1 = 0.0143, wR2 = 0.0330
R indices (all data)	R1 = 0.0146, wR2 = 0.0332
Absolute structure parameter	-0.034(9)
Extinction coefficient	0.0145(8)
Largest diff. peak and hole	0.238 and -0.245 e.Å ⁻³

Supplementary Table 1. Single crystal refinement parameters of the K₂Ni₂(SO₄)₃ structure at 100 K

	x	y	z	U(eq)	Site
Ni(1)	1645(1)	1645(1)	1645(1)	5(1)	4a
Ni(2)	5945(1)	945(1)	4055(1)	5(1)	4a
K(1)	1854(1)	-1854(1)	3146(1)	10(1)	4a
K(2)	4507(1)	4507(1)	4507(1)	10(1)	4a
S(1)	2826(1)	1233(1)	4806(1)	5(1)	12b
O(1)	2550(2)	952(2)	3371(2)	12(1)	12b
O(2)	2581(2)	-28(2)	5572(2)	15(1)	12b
O(3)	4246(2)	1699(2)	4987(2)	10(1)	12b
O(4)	1907(2)	2262(2)	5371(2)	13(1)	12b

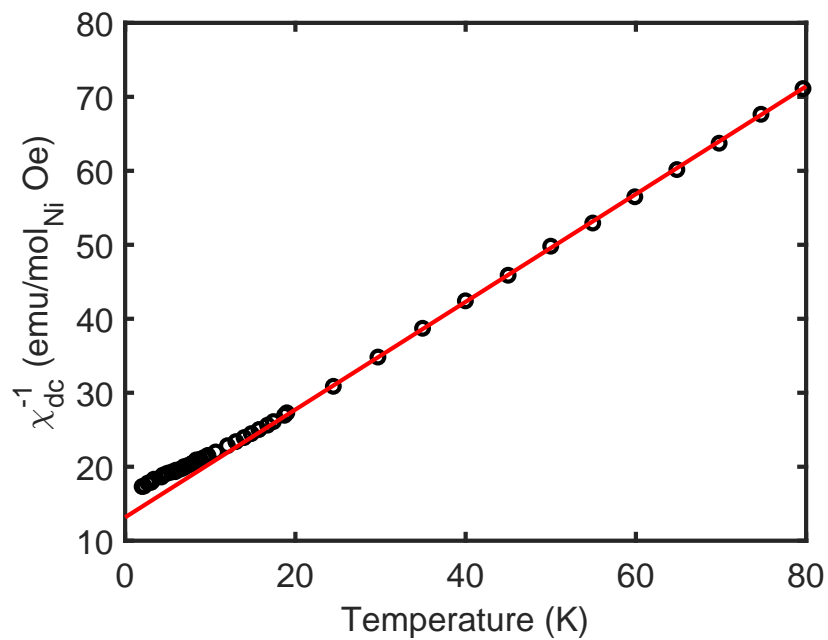
Supplementary Table 2. Fractional atomic coordinates ($\times 10^4$) and equivalent isotropic displacement parameters ($\text{Å}^2 \times 10^3$) for K₂Ni₂(SO₄)₃ at 100 K. $U(eq)$ is defined as one third of the trace of the orthogonalized U_{ij} tensor.

Ni(1)-K(1)	3.7435(3)
Ni(1)-O(1)	2.0315(18)
Ni(2)-K(2)	3.7977(4)
Ni(2)-O(3)	2.0417(18)
K(1)-O(1)	2.847(2)
K(1)-O(2)	3.065(2)
K(2)-O(3)	2.8094(19)
S(1)-O(1)	1.4613(18)
S(1)-O(2)	1.469(2)
S(1)-O(3)	1.4782(18)
S(1)-O(4)	1.4636(18)
O(1)-Ni(1)-K(1)	48.72(6)
O(3)-Ni(2)-K(2)	46.38(5)
O(1)-K(1)-O(2)	47.00(5)
K(1)-S(1)-K(2)	146.85(2)
O(1)-S(1)-K(1)	49.47(8)
O(1)-S(1)-K(2)	100.00(8)
O(1)-S(1)-O(2)	107.72(12)
O(1)-S(1)-O(3)	110.41(11)
O(1)-S(1)-O(4)	112.40(11)
O(2)-S(1)-K(1)	58.29(9)
O(2)-S(1)-K(2)	149.72(9)
O(2)-S(1)-O(3)	110.71(11)
O(3)-S(1)-K(1)	124.71(7)
O(3)-S(1)-K(2)	46.05(7)
O(4)-S(1)-K(1)	126.40(8)
O(4)-S(1)-K(2)	72.52(8)
O(4)-S(1)-O(2)	106.69(12)
O(4)-S(1)-O(3)	108.85(11)
Ni(1)-O(1)-K(1)	98.86(7)
S(1)-O(1)-Ni(1)	145.35(12)
S(1)-O(1)-K(1)	107.57(10)
S(1)-O(2)-K(1)	97.65(10)
Ni(2)-O(3)-K(2)	101.88(7)
S(1)-O(3)-Ni(2)	127.24(10)
S(1)-O(3)-K(2)	111.68(9)

Supplementary Table 3. Bond lengths (in Å) and angles (in degrees) for $\text{K}_2\text{Ni}_2(\text{SO}_4)_3$ at 100 K.

MAGNETIZATION

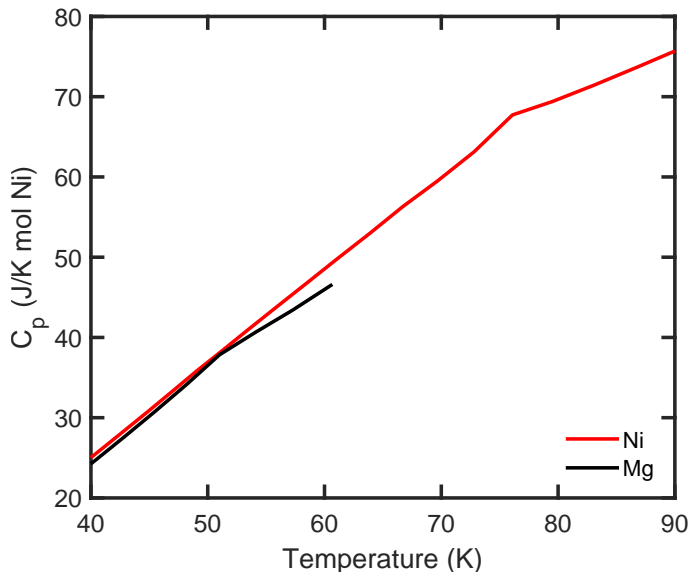
Low temperature view of the temperature dependence of the inverse of magnetic susceptibility $\chi_{dc} = M/B$. A weak deviation from the Curie-Weiss law starts below 50 K but it is significantly visible only below 20 K.



Supplementary Figure S3. Deviation from the Curie-Weiss law.

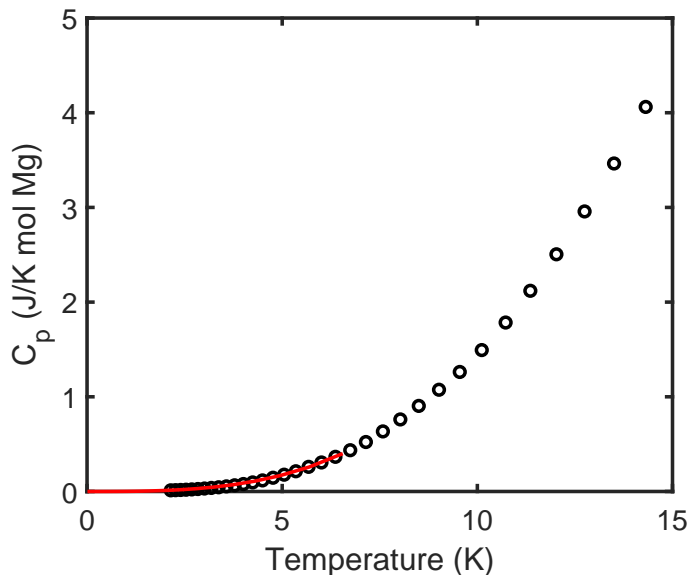
SPECIFIC HEAT

As shown in Supplementary Figure S4, at higher temperatures both $\text{K}_2\text{Ni}_2(\text{SO}_4)_3$ and the non-magnetic analog $\text{K}_2\text{Mg}_2(\text{SO}_4)_3$ show kinks in their specific heat. These are probably related to the freezing of SO_4 groups without a noticeable symmetry lowering from the cubic space group.



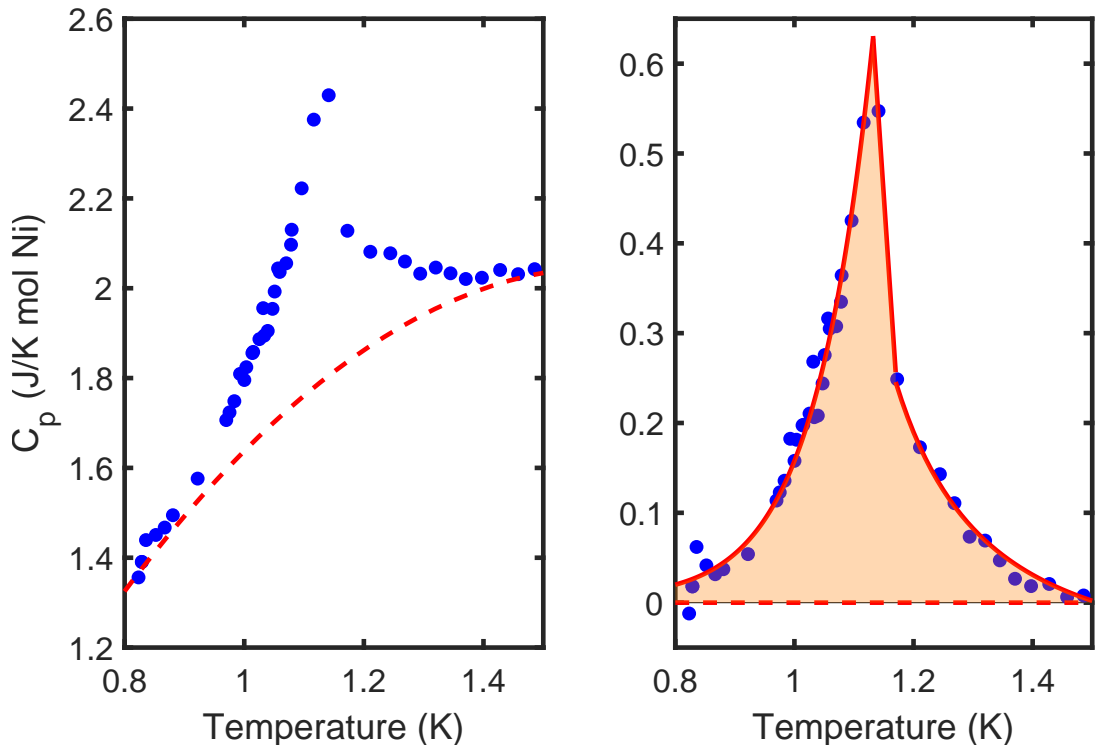
Supplementary Figure S4. Kinks in the specific heat of $\text{K}_2\text{Ni}_2(\text{SO}_4)_3$ and $\text{K}_2\text{Mg}_2(\text{SO}_4)_3$.

The phonon contribution below 2 K has been estimated by employing a polynomial $BT^3 + CT^5$ with $B = 1.33(3) \cdot 10^{-3} \text{ J/mol K}^4$ and $C = 2.1(8) \cdot 10^{-6} \text{ J/mol K}^6$ that best matches the measured specific heat of $\text{K}_2\text{Mg}_2(\text{SO}_4)_3$ at low temperatures, as seen in Supplementary Figure S5.



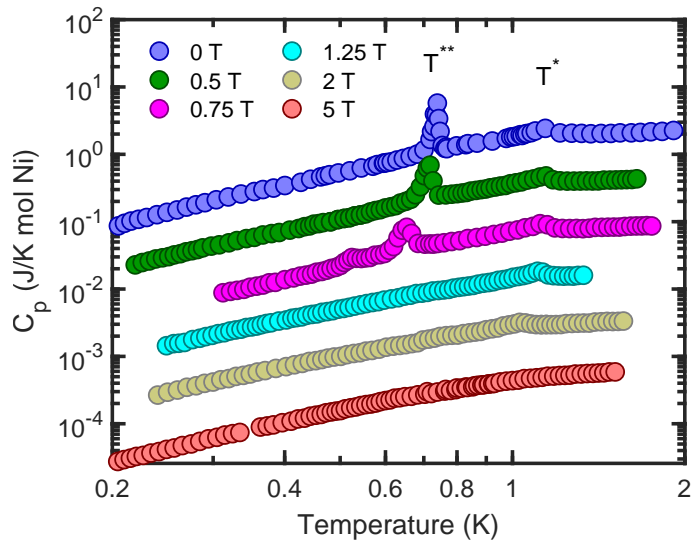
Supplementary Figure S5. Specific heat of $\text{K}_2\text{Mg}_2(\text{SO}_4)_3$ with a low temperature extension based on a polynomial $BT^3 + CT^5$.

Determination of specific heat involved in the second order phase transition at T^* is displayed in Supplementary Figure S6. The red curved dashed line is the measurement at 5 T where no anomaly is present, adjusted to match the zero-field data at 0.8 K and 1.5 K. The exact position of the background line does not change significantly the extracted value of $\sim 1\%$ of the total $R\ln(3)$ entropy of spin-1 system.



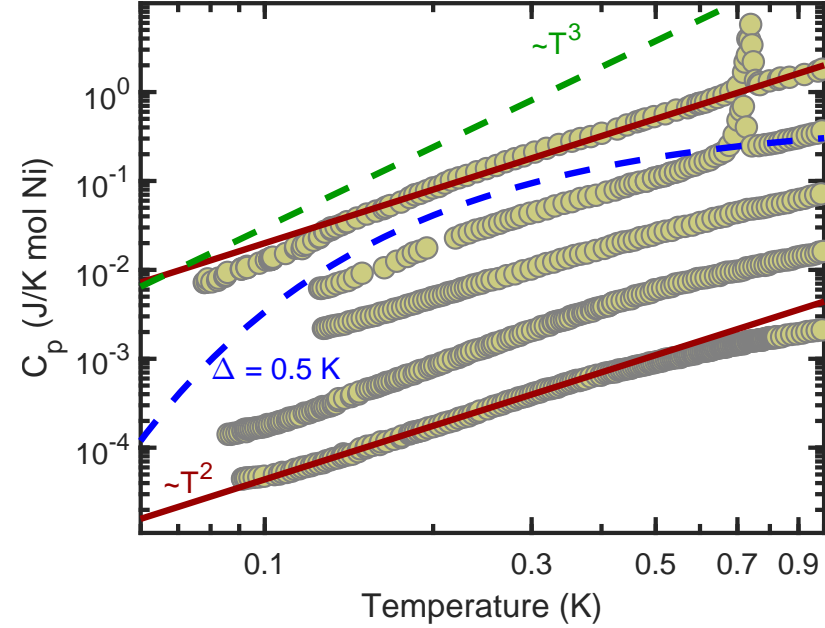
Supplementary Figure S6. Second order transition at T^* . The shaded area carries an entropy of $\sim 1\%$ of the total $R\ln 3$.

Magnetic field evolution of T^* and T^{**} is presented in Supplementary Figure S7. For $B = 0.75$ T a small shoulder appears around 0.5 K, possibly indicating another phase. Given that this is seen for a very narrow magnetic field range, it could also reflect an experimental artifact.



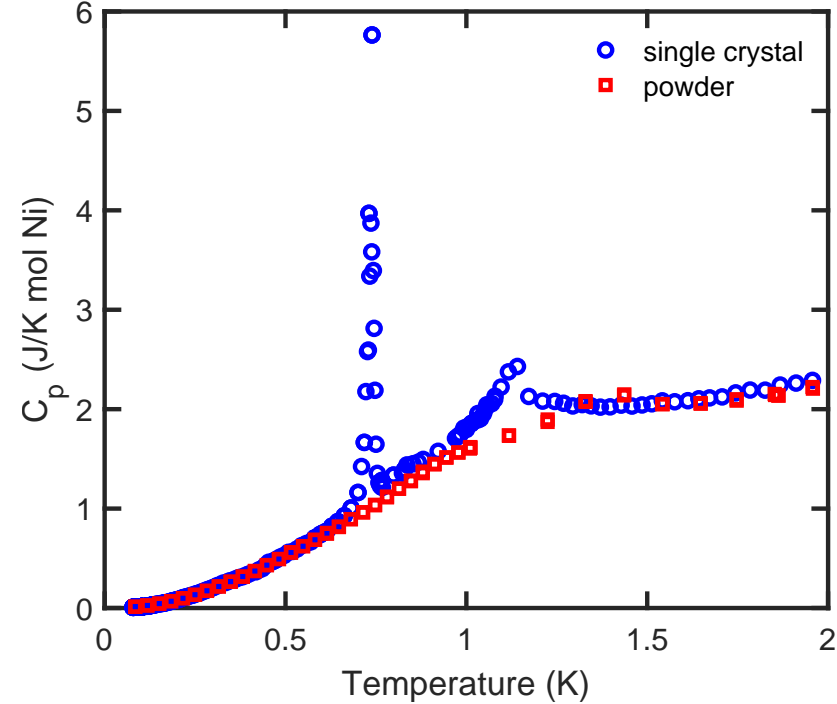
Supplementary Figure S7. Magnetic field dependence of specific heat below 2K. Individual curves are shifted vertically for clarity.

Comparison of a power-law behavior $C_P \sim T^n$ for $n = 2$ and $n = 3$ with a gaped behavior $C_P \sim \exp(-\Delta/T)$ is presented in Supplementary Figure S8. Zero field data show a somewhat varying slope, possibly influenced by the presence of the static component. $\Delta = 0.5$ K corresponds to the value of a spin-triplet gap for a static dimer on the J_4 bond.



Supplementary Figure S8. Low temperature specific heat for magnetic field values $B = 0, 0.5, 1.5, 7$ and 14 T (top to bottom). Individual curves are shifted vertically for clarity.

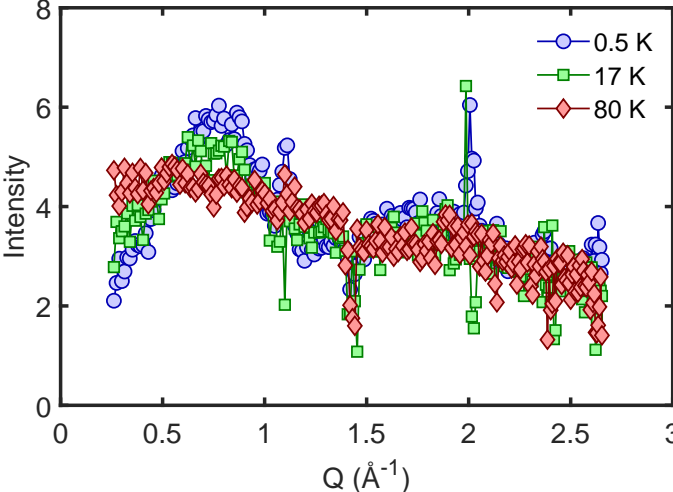
Comparison between results of specific heat obtained on single crystal and on powder samples is shown in Supplementary Figure S9.



Supplementary Figure S9. Comparison between single crystal and powder measurements.

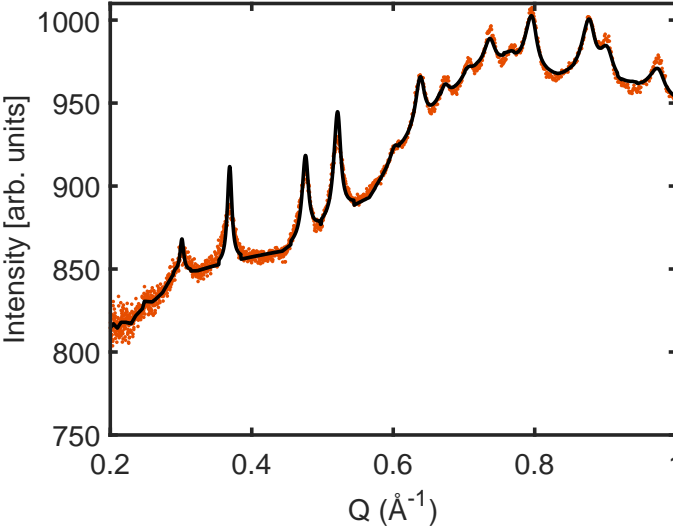
NEUTRON SCATTERING

In Fig. S10 we show the temperature dependence of the scattering profile of polarized neutrons. At 17 K the period of oscillations is still visible, although with a smaller amplitude. At 80 K the profile is practically featureless. The spikes occur at positions of nuclear Bragg peaks and are related to imperfect subtraction of large numbers in spin-flip and non-spin-flip channels.



Supplementary Figure S10. Temperature dependence of spin-polarized neutron diffraction.

Fig. S11 displays the diffraction data at 90 mK together with a LeBail fit using three propagation vectors $Q_1 = (\frac{1}{3}, 0, 0)$, $Q_2 = (\frac{1}{3}, \frac{1}{3}, 0)$ and $Q_3 = (\frac{1}{3}, \frac{1}{3}, \frac{1}{3})$. For $Q > 1 \text{ \AA}$ the satellites appear as shoulders of strong nuclear Bragg peaks which together with a diminishing form factor makes them very hard to distinguish.

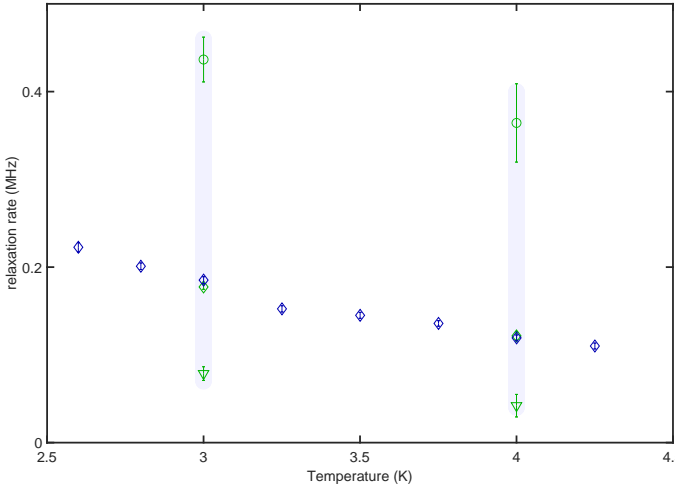


Supplementary Figure S11. Low-Q diffraction profile of $K_2Ni_2(SO_4)_3$ at 90 mK (points) with a Leball fit (line).

MUON SPIN RELAXATION

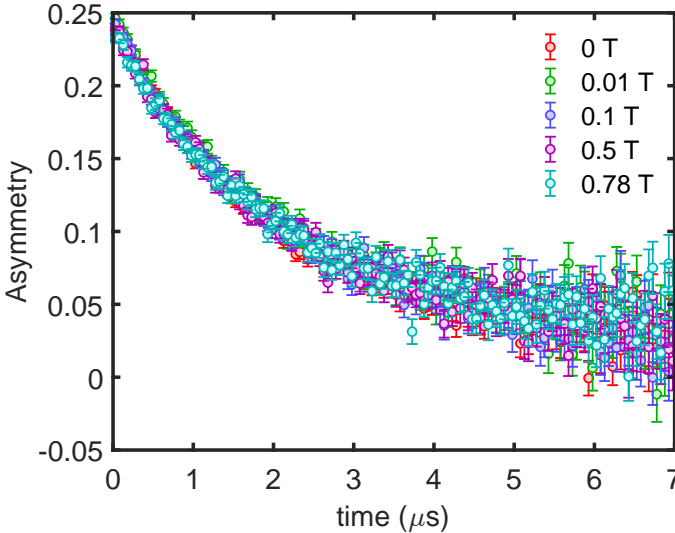
Taking into account that the whole data set is measured with two different experimental setups (a dilution refrigerator and a variable temperature insert, implying different backgrounds and different initial asymmetries), the temperature evolution of relaxation rates and exponents are presented in two segments. The low temperature segment, from 20 mK up to 4 K, is modeled using Eq.(2) from the main text, while the high temperature segment, from 100 K down to 3 K, is modeled using Eq.(1). In the region around 3 K both approaches can be used so if the low temperature segment is modeled using Eq.(1), the extracted relaxation rates overlap, as shown in Fig. S12 with green and blue diamonds.

It is rather simple to understand why two approaches work equally well. In this overlapping region the exponent β acquires values close to 1, rendering two contributions in Eq.(2) identical and effectively becoming Eq.(1). For two approaches to smoothly transform from one to the other it would be necessary to allow for the fraction f and β_1 to be freely varied or that a microscopic model is developed which could meaningfully constrain other parameters.



Supplementary Figure S12. Temperature region where two segments are equally well described with both equations (see main text).

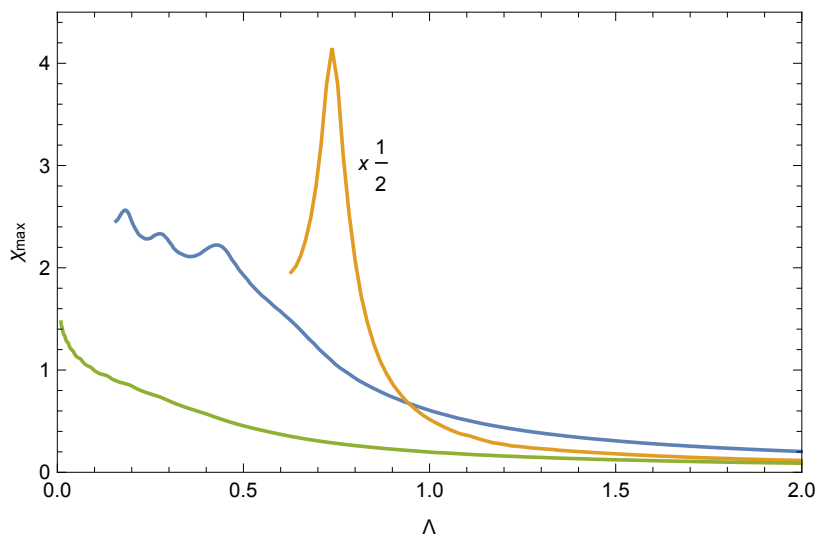
Fig. S13 shows longitudinal-field μ SR relaxation at 1.7 K, well within the correlated region. The system remains dynamic with fields up to 0.78 T.



Supplementary Figure S13. Longitudinal-field μ SR relaxation at 1.7 K.

ADDITIONAL PFFRG INFORMATION

In PFFRG the magnetic susceptibility depends on the renormalization group parameter Λ which is implemented as a sharp infrared frequency cutoff. Despite the artificial nature of Λ it shows various similarities with the temperature T , particularly, kinks or cusps in the Λ -dependence of the susceptibility signal the onset of magnetic long-range order. Most importantly, the identification of either magnetic long-range order or a magnetically disordered phase does not rely on any prior assumption on the system's ground state. To illustrate the identification of magnetic order, Fig. S14 shows the maximal susceptibility in momentum space as a function of Λ for various different systems. The orange curve corresponds to a spin-1 Heisenberg model on the lattice network of $\text{K}_2\text{Ni}_2(\text{SO}_4)_3$ but with $J_4 > 0$ interactions only. The antiferromagnetic Néel order in this system manifests in a strong peak. On the other hand, the green curve is a typical example for a smooth non-magnetic renormalization group flow as given for the spin-1/2 nearest neighbor antiferromagnetic Heisenberg model on the pyrochlore lattice. The PFFRG data for $\text{K}_2\text{Ni}_2(\text{SO}_4)_3$ is presented by the blue curve and shows an intermediate behavior: A small kink at $\Lambda \approx 0.45$ is observed which, however, does not develop into a pronounced peak (note that small oscillations below $\Lambda \approx 0.45$ are typically artifacts of the discretization of continuous frequency variables within our numerics). This indicates that our PFFRG results are in accord with a small ordered moment in the absence of an external magnetic field.



Supplementary Figure S14. Maximal susceptibility in momentum space as a function of the renormalization group parameter Λ from PFFRG. The green curve is an example for a non-magnetic system (spin-1/2 nearest neighbor antiferromagnetic Heisenberg model on the pyrochlore lattice). The orange curve represents a magnetically ordered system (spin-1 Heisenberg model on the double trillium lattice with $J_4 > 0$ couplings only). The blue curve represents the data for $\text{K}_2\text{Ni}_2(\text{SO}_4)_3$.

* ivica.zivkovic@epfl.ch

- [1] K. Koepnik and H. Eschrig, *Phys. Rev. B* **59**, 1743 (1999).
- [2] J. P. Perdew, K. Burke, and M. Ernzerhof, *Phys. Rev. Lett.* **77**, 3865 (1996).
- [3] A. I. Liechtenstein, V. I. Anisimov, and J. Zaanen, *Phys. Rev. B* **52**, R5467 (1995).
- [4] H. O. Jeschke, F. Salvat-Pujol, E. Gati, N. H. Hoang, B. Wolf, M. Lang, J. A. Schlueter, and R. Valentí, *Phys. Rev. B* **92**, 094417 (2015).
- [5] H. O. Jeschke, H. Nakano, and T. Sakai, *Phys. Rev. B* **99**, 140410 (2019).
- [6] T. Mizokawa and A. Fujimori, *Phys. Rev. B* **54**, 5368 (1996).
- [7] J. Reuther and P. Wölfle, *Phys. Rev. B* **81**, 144410 (2010).
- [8] M. L. Baez and J. Reuther, *Phys. Rev. B* **96**, 045144 (2017).
- [9] J. Polchinski, *Nucl. Phys. B* **231**, 269 (1984).
- [10] C. Wetterich, *Phys. Lett. B* **301**, 90 (1993).